

1 **Ultralong one-dimensional plastic zone created in aluminum underneath**  
2 **a nanoscale indent**

3 Zhi-Yu Nie<sup>1</sup>, Yuji Sato<sup>2</sup>, Shigenobu Ogata<sup>3</sup>, Maria Jazmin Duarte<sup>4</sup>, Gerhard Dehm<sup>4</sup>, Ju Li<sup>5</sup>,  
4 Evan Ma<sup>6</sup>, De-Gang Xie<sup>1\*</sup>, Zhi-Wei Shan<sup>1\*</sup>

5 <sup>1</sup> *Center for Advancing Materials Performance from the Nanoscale (CAMP-Nano), State*  
6 *Key Laboratory for Mechanical Behavior of Materials, Xi'an Jiaotong University, Xi'an*  
7 *710049, China.*

8 <sup>2</sup> *Department of Mechanical Engineering, The University of Tokyo, Tokyo 113-8656, Japan*

9 <sup>3</sup> *Department of Mechanical Science and Bioengineering, Osaka University, Osaka 560-*  
10 *8531, Japan.*

11 <sup>4</sup> *Max-Planck-Institut für Eisenforschung GmbH, Düsseldorf 40237, Germany.*

12 <sup>5</sup> *Department of Nuclear Science and Engineering and Department of Materials Science*  
13 *and Engineering, Massachusetts Institute of Technology, Cambridge, Massachusetts*  
14 *02139, USA*

15 <sup>6</sup> *Center for Alloy Innovation and Design, State Key Laboratory for Mechanical Behavior*  
16 *of Materials, Xi'an Jiaotong University, Xi'an, China.*

17 \* Corresponding authors e-mail: [dg\\_xie@xjtu.edu.cn](mailto:dg_xie@xjtu.edu.cn), [zwshan@mail.xjtu.edu.cn](mailto:zwshan@mail.xjtu.edu.cn)

20

21 **ABSTRACT:** Nanoindentation on crystalline materials is generally believed to generate a  
22 three-dimensional dislocation-dominated plastic zone, which has a semi-spherical shape with  
23 a diameter no larger than a few times the indentation depth. Here, by observing  
24 nanoindentation on aluminum *in situ* inside a transmission electron microscope, we  
25 demonstrate that the conventional three-dimensional plasticity dominated by regular  
26 dislocations triumph as the contact size upon yielding increases above  $\sim 100$  nm. However,  
27 when the contact diameter is less than  $\sim 50$  nm, a narrow and long (hereafter referred to as  
28 “one dimensional”) plastic zone can be created in front of the tip, as the indenter successively  
29 injects prismatic dislocation loops/helices into the crystal. Interestingly, this one-dimensional  
30 plastic zone can penetrate up to hundred times the indentation depth, far beyond the  
31 prediction given by the Nix-Gao model. Our findings shed new light on understanding the  
32 dislocation behavior during nanoscale contact. The experimental method also provides a  
33 potentially novel way to interrogate loop-defects interactions, and to create periodic loop  
34 arrays at precise positions for the modification of properties (e.g., strengthening).

35 **KEYWORDS:** Nanoindentation; Indentation size effect; Dislocation structure; In situ  
36 TEM; Incipient plasticity;

## 37 1. Introduction

38 Quantitative mechanical measurements using nanoindentation or atomic force  
39 microscopy (AFM) are powerful in probing crystal plasticity at the nanoscale. The  
40 displacement burst (or “pop-in”)[1-6] offers useful information regarding the nucleation and  
41 propagation of dislocations involved in initial yielding. In nanoindentation testing, the stress  
42 distribution produced by the indenter is not uniform, with the stress level decreasing rapidly  
43 with increasing distance from the local region under the indenter, generating a three-  
44 dimensional hemispherical stress field[7]. As a result, the generation and propagation of  
45 dislocations in the hemispherical region produce a corresponding plastic zone. Such a three-  
46 dimensional plastic zones (3D PZ) has been repeatedly verified by numerous experimental  
47 characterizations of dislocations using commercially available indenters[8-10]. However,  
48 this picture is unlikely to hold when the indenter tip has an extraordinarily small size, such  
49 as a diameter less than ~20 nm. Recent atomistic simulations[11-13] and experimental  
50 results[14-16] suggest that the plastic zone then consists of prismatic dislocation loops  
51 (PDLs), propagating deep into the crystal being probed. Compared with regular dislocations,  
52 dislocation loops (including both PDLs and helical loops) have some special characteristics.  
53 First, since the Burgers vector of a PDL is perpendicular to the loop plane, the size and slip  
54 path of a PDL is strongly confined by a prismatic slip tunnel. The PDL can only glide along  
55 one slip direction, as described by Ashby et al.[17]. Second, the glide of prismatic loops  
56 involves no dislocation intersection and reaction. Therefore, the stacked dislocation loop can  
57 preserve its configuration throughout the test and penetrate to a large depth below the surface.  
58 By contrast, regular dislocations can easily change their line length and slip plane by cross-

59 slip, so that they spread to form roughly a hemispherical distribution. The PDLs may thus  
60 lead to a distinctly different plastic zone, in terms of its make-up and morphology. There is  
61 a pressing need to explore what happens in this case, especially since mechanical tests are  
62 moving towards nanometer scale, such as in the atomic force microscopy (AFM) based  
63 nanoindentation [18-20]. An understanding of this scenario is also important for developing  
64 appropriate plastic mechanics models for nanoscale contacts.

65 *In situ* testing inside a transmission electron microscope (TEM) is an informative  
66 technique to reveal the dislocation evolution during nanoindentation. To this end, previous  
67 experiments [15, 16, 21, 22] have attempted the use of a nanoscale indenter, but the shape/size  
68 of the indenter tip was not well defined. Here we employ an *in situ* TEM nanoindentation  
69 experimental set up (**Fig. 1**), with indenter tips that have a well-defined spherical apex. The  
70 tip radius ranges from 8 to 150 nm, to cover the size regime of interest. Flat single crystalline  
71 aluminum plates offer ample sample volume to accommodate dislocation generation and  
72 propagation during nanoindentation. Moreover, to meet the “pristine crystal” assumption in  
73 the nanoindentation, the aluminum plates were well annealed to remove most, if not all,  
74 preexisting dislocations before engaging the tip, so that all the observed dislocations are  
75 freshly generated and their subsequent evolution is undisturbed by preexisting defects. In the  
76 following, we will show that the plastic zone transitions from 3D to 1D, depending on the  
77 contact diameter: when the contact diameters were larger than  $\sim 100$  nm, a fully developed  
78 three-dimensional plastic zone (3D PZ) consisting of regular dislocations was observed.  
79 When the contact diameter was less than  $\sim 50$  nm, we demonstrate a novel one-dimensional  
80 plastic zone (1D PZ) consisting of one single PDL array extending along the indent direction  
81 up to 150 times of the indentation depth below the contact surface. In between these two

82 sizes, the plastic zone is a mixture of the 1D and 3D types. Our results from molecular  
83 dynamics (MD) simulation further corroborate that the stress field generated by the indenter  
84 is the decisive factor to the geometry of the plastic zone.

## 85 **2. Experiments and Methods**

86 **Sample preparation:** A single crystal pure aluminum (99.9995%) disk was incised into  
87  $1.5 \times 2 \times 0.5 \text{ mm}^3$  rectangular plates, which was then mechanically polished to  $\sim 100 \text{ }\mu\text{m}$  in  
88 thickness and electrochemically thinned to a few microns. After the thinning, the aluminum  
89 plates were attached to the sample holder using conductive epoxy with high temperature  
90 compatibility. Before curing the epoxy, the orientation of the aluminum plates was carefully  
91 adjusted such that the indentation direction will be precisely aligned along [110] in the  
92 ensuing tests. Then, rectangular plates with thickness of  $\sim 500 \text{ nm}$  were fabricated using focus  
93 ion beam (FEI Helios600), and the end surface was also polished flat with its normal aligned  
94 with the loading direction. Before nanoindentation tests, the aluminum plates were annealed  
95 at  $400 \text{ }^\circ\text{C}$  for at least 30 min in vacuum to remove lattice defects and obtain an approximately  
96 pristine interior.

97 ***In situ* TEM nanoindentation experiments.** The *in situ* TEM nanoindentation  
98 experiments were performed with Hysitron PI95 ECR Picoindenter in a JEM-2100F  
99 transmission electron microscope (operated at 200 kV). The indenters were made from a  
100 tungsten rod by using the focus ion beam to machine one end into a pyramidal tip with the  
101 spherical apex (radius=8 to 150 nm). We used displacement control at the loading rate of  $\sim 2$   
102 nm/s during indentation, and the resultant evolution of dislocation was recorded as movies  
103 with a Gatan 830(SC200) CCD camera at frame rate=10 fps.

104           **Method of nanoindentation MD simulation.** Atomic model of FCC Al with  
105 orientations —  $x: [\bar{1}\bar{1}\bar{2}]$ ,  $y: [\bar{1}\bar{1}1]$ ,  $z: [110]$  — was constructed. The dimension of the model  
106 was  $70.4 \text{ nm} \times 70.6 \text{ nm} \times 304.0 \text{ nm}$ . The number of atoms was 91,387,224. The embedded  
107 atom method (EAM) potential for Al[23] was used to describe the interatomic interactions.  
108 The lattice constants and elastic constants were estimated as  $b = 4.05 \text{ \AA}$ ,  $C_{11} = 114$ ,  $C_{12} =$   
109  $61.6$ , and  $C_{44} = 31.6 \text{ GPa}$ , which agree with the experimentally determined values of  $b = 4.05$   
110  $\text{ \AA}$ ,  $C_{11} = 114$ ,  $C_{12} = 61.9$ , and  $C_{44} = 31.6 \text{ GPa}$ . Before starting indentation simulations, the  
111 models were first equilibrated using Parrinello-Rahman NPT ensemble method[24] for 50 ps  
112 at an in-plane normal stress of 0 Pa at simulation temperatures of 300 K to release the in-  
113 plane stresses. The  $z$  position of the spherical indenter with radius  $R_{\text{sim}} = 8 \text{ nm}$  was controlled  
114 to move along an axis perpendicular to the model surface at 6 m/s. During the simulations,  
115 the center of mass of the atomic slab model was fixed and the  $x$  and  $y$  dimensions of the slab  
116 model were relaxed such that the normal stress was 0 Pa in these directions. The following  
117 repulsive force was assumed to act between the indenter and the slab model:  $F(r) = -K(r -$   
118  $R_{\text{sim}})^2$ ;  $r < r_c$ , where  $r$  denotes the distance of the atoms in the target material to the centroid  
119 of the spherical indenter tip,  $K$  denotes a force constant, which was set to  $10 \text{ eV/\AA}^3$ , and  $r_c$   
120 denotes the potential cut-off distance, which was set to 0.63 nm.

### 121   **3. Results and discussion**

#### 122    **3.1. Three-dimensional plastic zone (3D PZ).**

123           **Fig. 2** and **Movie S1** show the typical results from the *in situ* nanoindentation test with  
124 an indenter tip radius of 150 nm under displacement control mode at the loading rate of 2

125 nm/s. **Fig. 2a** is the quantitative data obtained during the nanoindentation, with the insert to  
126 show the initial shape of the indenter tip. The plot shows a clearly defined single pop-in event  
127 at the peak load of 118  $\mu\text{N}$ . As shown in **Fig. 2b**, the plate has a “pristine crystal” interior  
128 and the indentation direction is along the [220] crystalline direction. Before the pop-in the  
129 whole sample remained pristine without generating any dislocations underneath the indenter,  
130 even at the peak load just before the pop-in (**Fig. 2c**). Considering that the contact is between  
131 a sphere and a flat surface, it is reasonable to apply the Hertzian elastic contact model to  
132 estimate the maximum shear stress underneath the indenter:  $\tau_{max}=0.465P/\pi a^2$ , where  $P$  is the  
133 critical load and  $a$  is the critical contact radius. By correlating the  $p$ - $h$  curve and the image  
134 frames from the video, we measured the  $P$  and  $a$  value at the moments of peak loads (**Fig.**  
135 **2c**). By plugging both measured values into the equation, we estimate the critical shear  
136 stresses for pop-in can reach  $2.1 \pm 0.2$  GPa. The pop-in accompanied by the generation of  
137 numerous regular dislocation lines underneath the indenter, expanding in various directions.  
138 **Fig. 2d** presents the dark-field postmortem characterization taken with [020] diffraction  
139 vector. A region of high-density dislocations was developed just below the contact location.  
140 We can observe that the dislocations are mainly contained in a hemispherical zone, as  
141 outlined in **Fig. 2d**. The hemispherical plastic zone confirms the picture of 3D PZ generated  
142 using commercially available indenters as mentioned earlier. The radius of the zone of high-  
143 density dislocations is approximately 3 times larger than residual indentation radius. This  
144 value is close to that proposed by Durst et al[25], who empirically assumed the radius of the  
145 plastic zone should be 1.5 to 2.5 larger than the contact radius.

### 146 **3.2. Three-dimensional plastic zone plus one-dimensional plastic zone**

147           **(3D+1D PZ).**

148           Using a smaller tip with a lower corner angle can result in the emission of dislocation  
149 loops. The high-density dislocation region is then accompanied by a long extending loop  
150 array. As shown in **Fig. 3** and **Movie S2**, an indenter with the tip radius of  $\sim 25$  nm was used  
151 to engage on the aluminum surface along the same crystallographic direction [220]. The  
152 corresponding quantitative mechanical data ( $p$ - $h$  curve) is shown in **Fig. 3a**; only one yielding  
153 event can be clearly defined at the time  $t_p$ . Before the yielding point, we only observed an  
154 expanding semi-ellipse-shaped strain contour that expands with increasing load, indicating a  
155 purely elastic deformation without emitting dislocations. The stress drops at the peak load of  
156  $22 \mu\text{N}$  relates to the generation of abundant dislocations loops and regular dislocations (**Fig.**  
157 **3b**). As exemplified in **Fig. S2**, this peak load corresponds to the critical shear stress for  
158 yielding of  $3.6 \pm 0.7$  GPa. This shear stress is on the order of the theoretical shear strength of  
159 the aluminum, estimated using  $G/2\pi$ , where  $G$  is the shear modulus (27 GPa for Al). Such a  
160 high stress is sufficient for the dislocation to nucleate homogeneously within the perfect  
161 lattice, although the effects of oxide film on the high stress could not be completely excluded.  
162 Unfortunately, at the high stress the dislocation generation processes are too fast to be caught  
163 by the camera. The bright-field image of **Fig. 3c** clearly shows the distribution of the resultant  
164 dislocations. One single loop array extended to  $\sim 2.7 \mu\text{m}$  beneath the indenter, comprising of  
165 a coaxial stack of prismatic/helical dislocation loops led by two individual PDLs.  
166 Morphologically, such a long extending plastic zone consisting of dislocation loops has the  
167 appearance of a one-dimensional plastic zone (1D PZ). In addition to this, near the indented  
168 surface there is also a hemispherical volume of jammed regular dislocations (3D PZ).



### 169 3.3. One-dimensional plastic zone (1D PZ).

170 With the indenter tip radius going further down, the indentation becomes more inclined  
171 to generate individual loops. The 1D PZ thus becomes dominating. **Fig. 4** and **Movie S3**  
172 show the results from such an indentation experiment using a tip with apex radius of  $\sim 15$  nm  
173 and corner angle of 60 degrees. The  $p$ - $h$  curve includes four displacement bursts, marked as  
174 P1-P4 in **Fig. 4a**. By correlating these displacement bursts with the microstructural evolution  
175 in the movie, as shown in **Fig. 4c-d**, the first two displacement bursts (P1-P2) can be related  
176 to the generation of PDLs that pile up in a row along [220], which is the slip direction of  
177 dislocations in aluminum, while in the third displacement burst P3, a few loops are emitted  
178 first and then some regular dislocations follow, and the ensuing fourth displacement burst  
179 (P4) only generates regular dislocations. **Fig. 4d** shows a full picture of dislocations  
180 remaining under the indenter after indentation. There are three different types of dislocations,  
181 i.e. the PDLs mainly in the form of single loops, the helical loops with each one involving  
182 two or more loops, and the regular dislocations. These different dislocations are generated  
183 through transition stages: in the middle of P3, the individual PDLs first transition to helical  
184 dislocations, which further transition to regular dislocations at the end of P3. As shown in  
185 **Fig. 4d**, the leading loop slips to a depth of 3400 nm before the gliding stops, even though  
186 the indentation depth is as small as 22 nm at the moment of P3. The penetration depth is 150  
187 times of the indentation depth, and thus far beyond the prediction by the Nix-Gao model  
188 where all the generated dislocations are contained in a hemisphere with the radius comparable  
189 to the indent radius[8, 9, 26]. The behavior of PDLs has been hypothesized before and also  
190 been observed in some other types of experiments, such as the growth of a spherical particle

191 in a solid matrix[27, 28]. However, ours is the first time to directly observe what actually  
 192 happens underneath a nanoindenter. The one published by Lee et al.[16] used an inverse  
 193 indenter rather than a normal indenter tip.

194 An elastic stage precedes each yielding event. The elastic stage shows a continuous  
 195 increase of the load with indentation depth and also is corroborated with the unchanged  
 196 dislocation configuration below the contact area during load rise. According to the Hertzian  
 197 elastic contact model we estimate the critical shear stresses for each yielding event, shown  
 198 as red points in **Fig. 4b** (as exemplified in **Fig. S2**). The  $\tau_{max}$  at the point P1 and P2 is as high  
 199 as  $\sim 2.7$  and  $2.6$  GPa, respectively, close to the ideal shear strength of aluminum, suggesting  
 200 that the contact is made with a nearly ideal flat plane and homogenous dislocation nucleation  
 201 is the preferred mechanism to initiate plasticity. However, in the P3 and P4 that follow, the  
 202 previously nucleated dislocations act as preexisting dislocations and the generated surface  
 203 steps may lead to high local stress concentration, such that the stress drops substantially to  
 204  $\sim 1.7$  GPa and  $\sim 1.2$  GPa. What's more, the stress drops associated with the transition from  
 205 the nucleation of dislocation loops to regular dislocation, this result indicates that the  
 206 nucleation of regular dislocations is more likely to be dominated by heterogeneous  
 207 dislocation nucleation, in contrast with the high stress required for the homogenous  
 208 nucleation of small closed dislocation loops.

### 209 **3.4. Configuration of the one-dimensional loop array.**

210 In a PDL array, the position of a loop is determined by the equilibrium between the  
 211 repulsive force exerted by other loops and the lattice friction. The repulsive force between  
 212 loops ( $P_{rz}$ ) is short-ranged[29], decreasing fast with the inter-loop spacing  $z$  following the  
 213 relation  $P_{rz} = br^3G/(1 - \nu)z^4$ , where  $G$  is the shear modulus,  $b$  is the magnitude of the

214 Burgers vector,  $r$  is the loop radius, and  $\nu$  is Poisson's ratio. The experimental observations  
215 indicate that the spacing between loops is comparable with their diameters. Consequently,  
216 the repulsive force that a loop feels from the loops farther than its third neighbor is almost  
217 negligible (the repulsive force from the first and second neighbors accounting for 94 % of  
218 the sum). This means that the spacing between two loops is largely dictated by the nearest  
219 two or three loops. Another conclusion from the above analysis is that when the glide of a  
220 dislocation loop in an array is driven by the elastic stress field of the previous one, dislocation  
221 motion can be easily transferred onwards. Specifically, when a new dislocation loop is  
222 emitted from the indentation site and squeezed into the row, a net repulsive stress between  
223 loops will be generated to push the nearest loop forward, which in the same way continues  
224 to push the next one. This action is repeated like a moving wave that propagates from the tail  
225 of the loop array to the leading loop. In this way, although the indentation stress field only  
226 provides a high driving stress in a small hemispherical volume, the plasticity can be  
227 transmitted over a long-distance, enabled by the re-lay of dislocation loops constituting the  
228 array. Therefore, although the elastic stress field imposed by the indenter is only able to drive  
229 regular dislocations to a distance comparable to the contact size, the glide of dislocation loops  
230 in an array can be sustained over a long distance. This explains our observation that the  
231 dislocation loops marched on like a group towards the deep interior of the aluminum crystal.  
232 Also derived from the force-chain mechanism is that the high stress around the indenter is  
233 not sustained unless/until the movement of the loop array is blocked by obstacles or  
234 heterogeneous dislocation nucleation sets in.

235 Moreover, the lattice friction stress ( $\tau_0$ ) can be extracted from the equilibrium configuration  
 236 of PDLs. Xin et al. suggested that the configuration of the loop array is determined by the  
 237 balance between the repulsive interaction between loops and the lattice friction stress ( $\tau_0$ )  
 238 opposing dislocation movement[30]. For an array of  $N + 1$  coaxial dislocation loops with  
 239 diameter  $d$ , the first leading loop is numbered 0 and the following loops is numbered  $i = 1 \sim N$   
 240 (**Fig. 5a**). If we define a normalized loop position:  $\zeta_i = (\Delta Z_i)/d$  ( $i = 1 \sim N$ ), where  $\Delta Z_i$   
 241 represents the distance between loop  $i$  and the loop 0. When the loop distance is large relative  
 242 to the loop size,  $\zeta_i$  can also be expressed as follow:

$$\zeta_i = \left( \frac{3\pi}{4\bar{d}} \right)^{\frac{1}{4}} \left\{ \frac{4}{3} [N^{3/4} - (N + 1 - i)^{3/4}] + \frac{1}{2} [N^{-1/4} + (N + 1 - i)^{-1/4}] + \frac{1}{48} [(N + 1 - i)^{-5/4}] \right\}$$
(1)

243 where the scaled loop size:

$$\bar{d} = 2\pi(1 - \nu)\tau_0 d / G|\mathbf{b}|$$
(2)

244 For the three sets of loop arrays with their average loop diameter of 33 nm, 60 nm, and 30  
 245 nm, respectively, the normalized loop position between each loop and the corresponding loop  
 246 0 was measured, as shown in **Fig. 5b**. We can then fit equation (1) for the measured loop  
 247 positions, to obtain the scaled loop size  $\bar{d}$ . By inserting reasonable parameters for aluminum  
 248 ( $\nu = 0.35$ ,  $G = 26$  GPa, and  $|\mathbf{b}| = 0.28$  nm) into equation (2), the lattice friction stress  $\tau_0$  can  
 249 thus be calculated as 1.22, 1.11 and 0.94 MPa for the three loop arrays, respectively.  
 250 Therefore, the averaged friction stress  $\tau_0 = 1.10 \pm 0.14$  MPa, close to the estimated value  
 251  
 252

253 for edge dislocations in Al by atomistic simulation ( $\sim 1$  MPa[31], 1.6 MPa[32] ) and  
254 mechanical tests (0.78 MPa[33], 1.05 MPa[34]).

### 255 **3.5. Size-dependent transition of plastic zones.**

256 Obviously, the transition of the plastic zone morphology is rooted in the size-dependent  
257 transition of self-closed loops to regular dislocations. In order to reveal the relation between  
258 contact sizes and dislocation types, the contact diameters and loop diameters are measured  
259 from the *in situ* video frames immediately after yielding events in several indentation tests  
260 with various indenter tip radii. The results are plotted as **Fig. 6**, which demonstrates that the  
261 loop size is nearly proportional to the contact diameter, by a factor of  $\sim 1.2$ . Besides, there are  
262 two threshold contact diameters, with  $D_{c1} \sim 50$  nm denoting the transition from the emission  
263 of PDLs to the generation of helices, and  $D_{c2} \sim 100$  nm for a transition between loop  
264 generation and nucleation of regular dislocations.

265 To explain the above two transitions from singular PDLs to helical loops to regular  
266 dislocations, we first need to understand the mechanism of nucleating a PDL. Previous  
267 research has observed the generation of PDL near a precipitation particle growing from a  
268 ductile metal matrix[17], which is supposed to be similar to the scenario in nanoindentation.  
269 The underlying mechanism of PDL nucleation during nanoindentation has also been studied  
270 by molecular dynamics (MD) simulations[13, 35, 36]. An well-accepted model suggests that  
271 due to the stress generated around the contact interface, a shear loop will nucleate first and  
272 bulge out on the  $\{111\}$  plane in response to the indentation stress field, when the shear stress  
273 is greatest on the adjacent  $\{111\}$  planes, the first cross-slip occurs. In the same way, the  
274 second cross-slip event occurs, bringing the segments back to the original slip plane. The

275 lasso-like dislocation loop with three sides of a parallelogram and a neck is generated from  
276 those two steps of cross slip processes. During the following slip, the screw segments of this  
277 neck attract and annihilate each other, resulting in the birth of an individual PDL. Despite of  
278 multiple atomistic modeling to show this process[12, 35-38], an experimental demonstration  
279 is still lacking. In another nanoindentation experiment, we also observed a similar process  
280 showing how an individual dislocation loop is generated near the contact interface. In **Fig. 7**  
281 and **Movie S4**, the generation of a PDL can be divided into four transient states. In the  
282 beginning, a half loop is nucleated from the contact interface and bows out in a (111) plane  
283 along the direction of [220] (**Fig. 7b**). In the following short period of 0.45 s, this half loop  
284 acts as an embryonic dislocation source from which seven PDLs are nucleated and injected  
285 into the crystal, a process too fast to be observed clearly. After emission of these loops, most  
286 of the stored elastic energy has been exhausted, and the dislocation nucleation process slowed  
287 down, thus allowing for catching some details of the next nucleation event. As shown in **Fig.**  
288 **7c**, the half loop developed into a lasso-like dislocation loop near the indenter. The neck of  
289 this lasso-like dislocation loop, as indicated by the pair of red arrows, became increasingly  
290 narrower with the rising load, until it shrank to a point and the dislocation segment under the  
291 neck pinched off to form an individual PDL (**Fig. 7d-e**).

292 It is noteworthy that multiple cross-slips and the reaction of shear dislocation segments  
293 are involved in the generation of a PDL, and both processes are highly sensitive to the local  
294 stress field. Therefore, we suggest that our observed transitions of dislocation configuration  
295 must be related to the effect of local stress field on dislocation nucleation. The formation of  
296 a closed prismatic loop depends on the symmetry of the indentation stress field. The  
297 simulation result shows that the cross slip occurs exactly where the force condition

298 changes[35, 39]. Therefore, the symmetry of the indentation stress field ensures that the two  
299 cross-slipped screw segments meet each other on the same slip plane, which is the mechanism  
300 for the loop to pinch off. If they miss each other, a helical loop will be generated. From this  
301 point of view, the generation of the individual closed loop is sensitive to the local stress  
302 fluctuations. After the pinching-off of PDL, the stress relaxes and the shear loop retracts  
303 back, returning to pristine state in the indent region. As the indentation proceeds, those PDL  
304 nucleation processes repeat. With the increase of contact area, to accommodate the lateral  
305 strain, the dislocations nucleation and propagation are also activated in the other two  $\langle 220 \rangle$   
306 directions. The intersection of the propagating directions provides the chances for the  
307 dislocations to meet and interact with each other, resulting in tangles or locks that reduce the  
308 dislocation mobility. The presence of dislocation near the contact interface can disturb the  
309 nucleation of dislocation loops, by changing the local elastic stress field to interrupt the  
310 closing-up of a loop or intermittently reacting with nucleated loops, thus leading to the  
311 creation of helical loops. As an increasing number of dislocations jam up near the contact  
312 area, the formation of individual dislocation loops finally becomes statistically impossible,  
313 and in the later stage, dislocation forest and mutual dislocation interactions (such as Frank–  
314 Read sources[12], dislocation unjamming[40, 41]) are presumed to be the dominant  
315 mechanism of plasticity. This transition process has also been observed in our own atomistic  
316 simulations: we conducted a molecular dynamics (MD) nanoindentation simulation on a  
317 (110) surface of cuboid-shaped Al atomistic model using 8 nm radius spherical indenter as  
318 shown in **Fig. 8**. The dislocation behavior during the nanoindentation simulation is recorded  
319 as a movie (**Movie S5**). It can be seen that with the expansion of the contact area and plastic  
320 zone, the structure of nucleated dislocations becomes more and more complex. Furthermore,

321 the distributions of resolved shear stress on the  $(1\bar{1}1)[110]$  slip system at the elastic and  
322 PDL emission stages (**Fig. 9a,b**) were symmetric, while those after the helical loop emission  
323 stage (**Fig. 9c,d**) lose such symmetry, and thus the distributions clearly illustrate the break-  
324 down of the symmetry of the indentation stress field at the generation of helical loops.

325 This picture of the dislocation evolution process has no significant anisotropic effects.  
326 When we change to another indentation direction, for example, along  $[1\bar{1}\bar{1}]$ , we observed  
327 similar dislocation evolution process, as shown in **Fig. 10** and **Movie S6**. As the contact  
328 radius increases, the transitions from individual PDLs to helical PDLs to jammed regular  
329 dislocation lines were also observed, similar to the observation in indentations along  $[220]$ .  
330 During this indentation experiment, a PDL array was punched into the crystal, and extended  
331 along the  $\langle 220 \rangle$  direction having the smallest angle with the indentation direction.

332 Previous theories and experimental characterizations show a consensus that the  
333 indentation only creates dislocations spreading in three dimensions, even in the early stage  
334 of the indentation[8, 21, 42]. What is more, in order to measure intrinsic film properties, a  
335 currently well-recognized empirical rule is that the indentation penetration depth must be less  
336 than 10% of the film thickness[43]. However, as we have observed, the plastic zone can  
337 extend in one dimension to a distance of several micrometers, realized by the fast glide of an  
338 array of small PDLs in the direction of their Burgers vector, even though the indentation  
339 depth is only  $\sim 20$  nanometers. This unusual penetration ability of the dislocation arrays is of  
340 significance for thin-film mechanical testing, considering that significant back stress can be  
341 built up to induce hardening when the movement of PDLs is impeded by substrate/film  
342 interface or some other obstacles. Our finding is even more important for applications using  
343 the atomic force microscope (AFM) with a tip radius of only a few nanometers[44, 45]



344 because such extraordinarily sharp indenter tip would generate PDLs, which have a high  
345 propensity to glide a large distance before piling up at obstacles.

346 In the following, we define a penetration ability factor for dislocations,  $f$ . For an array  
347 of dislocation loops, the penetration ability factor is evaluated as the distance from the first  
348 leading loop to the indented site divided by the indentation depth (solid circles in **Fig. 11**).  
349 For the regular dislocations residing in a hemispherical zone, we use the ratio between the  
350 fitted radius of this hemisphere and the indentation depth to represent the propagation ability  
351 factor (hollow circles in **Fig. 11**). In **Fig. 11** we summarized the results from a few indentation  
352 tests with tips of varying radius, to show the propagation ability factor for dislocations  
353 generated from different contact diameters in pop-in events. When the contact radius before  
354 yielding is smaller than  $\sim 80$  nm, we observed that the PDLs array could extend over one  
355 hundred times deeper than the penetration depth of the indenter, also ten times deeper than  
356 that predicted by the 10% empirical rule mentioned above[46]. However, for regular  
357 dislocations, the propagation ability factors are about ten. With the increase of the contact  
358 diameter, the regular dislocations would expand and gradually overwhelm the PDLs, which  
359 has stopped moving after the first few pop-ins. When the contact radius before yielding is  
360 larger than  $\sim 100$  nm, most of the dislocations generated during the indentation would be  
361 contained in a hemispherical volume with a radius ten times of the indentation depth. This  
362 indicates that the 10% empirical criterion is only valid for indentations using a relatively  
363 large indenter, or when the contact diameter significantly exceeds  $\sim 100$  nm.

#### 364 **4. Summary**

365 Our work raises several points that are worthy of attention and have potential impact.  
366 First, we note the observed early-stage plasticity induced by nanoscale contact is in fact a  
367 common occurrence, considering that commercially available nanoindentation tips usually  
368 start with an apex/asperity radius of a few tens of nanometers, let alone the much sharper tips  
369 used in AFM. Our observations therefore offer a new perspective into what could happen  
370 using the popular nanoindentation methodology. Second, our results shed new light on the  
371 indenter size effect, specifically on the form of indentation plastic zone, bridging previous  
372 predictions from atomistic simulations with experimental observations. Third, we found that  
373 the dislocation loops in the array can be pushed to travel a long distance. The probability for  
374 them to meet other preexisting obstacles and thus cause hardening is much higher than that  
375 expected from regular dislocations. This would be especially important for mechanical  
376 measurements on films with a thickness of a few micrometers or less, because the dislocation  
377 loops have the ability to reach and interact with the film/matrix interface, thus altering the  
378 properties being examined. One can observe abnormal size effects at very shallow  
379 indentation depth, effects that are not taken into account in the Nix-Gao model. Fourth, our  
380 experimental method provides a novel way to “focus” defects so as to interrogate their  
381 interactions, for example by impinging PDLs onto preexisting grain boundaries, phase  
382 boundaries or precipitate particles. One can also envision the use of a sharp indenter to  
383 implant dislocation loop arrays at desired places, one location at a time, setting up a grid  
384 pattern of obstacles to moving dislocations in the film for strengthening or other purposes:  
385 e.g. to pattern self-assembled low-dimensional nanostructures [26, 47]

386

**387 Declaration of Competing Interest**

388 The authors declare no competing financial interests.

**389 Author contributions**

390 Z.S. and E.M. supervised the project., Z.N., and D. X. designed the experiments. Z.N.  
391 conducted the experimental work. S.O. guided the MD modelling analysis. Y.S. conducted  
392 the MD simulations. Z.N., D.X., Z.S., and E.M. wrote the paper. All authors contributed to  
393 the discussions of the results.

**394 Acknowledgments**

395 We acknowledge P. Zhang, C. Y. B. Qin, and C. W. Guo (Xi'an Jiaotong University) for  
396 assistance in focused ion beam and TEM experiments. The authors acknowledge the supports  
397 from Natural Science Foundation of China (51971169, 52031011). We also appreciate the  
398 support from the International Joint Laboratory for Micro/Nano Manufacturing and  
399 Measurement Technologies and the Collaborative Innovation Center of High-End  
400 Manufacturing Equipment. Y.S. and S.O. acknowledge the Center for Computational  
401 Materials Science, IMR, Tohoku University for the use of MASAMUNE-IMR and the  
402 Cybermedia Center, Osaka University for the use of OCTOPUS. S.O. acknowledges the  
403 support by the JSPS KAKENHI Grant Nos. JP17H01238 and JP17K18827.

**404 Supporting Information**

405 Supplementary material associated with this article can be found in the online:

**406 References**

407 [1] T. Zhu, J. Li, Ultra-strength materials, Prog. Mater Sci. 55(7) (2010) 710-757.

- 408 [2] L.Y. Chen, M.R. He, J. Shin, G. Richter, D.S. Gianola, Measuring surface dislocation  
409 nucleation in defect-scarce nanostructures, *Nat Mater* 14(7) (2015) 707-13.
- 410 [3] T.A. Michalske, J.E. Houston, Dislocation nucleation at nano-scale mechanical contacts,  
411 *Acta Materialia* 46(2) (1998) 391-396.
- 412 [4] D. Lorenz, A. Zeckzer, U. Hilpert, P. Grau, H. Johansen, H.S. Leipner, Pop-in effect as  
413 homogeneous nucleation of dislocations during nanoindentation, *Physical Review B* 67(17)  
414 (2003).
- 415 [5] C.A. Schuh, J.K. Mason, A.C. Lund, Quantitative insight into dislocation nucleation from  
416 high-temperature nanoindentation experiments, *Nat Mater* 4(8) (2005) 617-21.
- 417 [6] Y. Sato, S. Shinzato, T. Ohmura, T. Hatano, S. Ogata, Unique universal scaling in  
418 nanoindentation pop-ins, *Nat Commun* 11(1) (2020) 4177.
- 419 [7] W.D. Nix, H. Gao, Indentation size effects in crystalline materials: a law for strain  
420 gradient plasticity, *Journal of the Mechanics and Physics of Solids* 46(3) (1998) 411-425.
- 421 [8] Y.L. Chiu, A.H.W. Ngan, A TEM investigation on indentation plastic zones in  
422 Ni<sub>3</sub>Al(Cr,B) single crystals, *Acta Materialia* 50 (2002) 2677-2691.
- 423 [9] L. Zhang, T. Ohmura, Plasticity initiation and evolution during nanoindentation of an  
424 iron-3% silicon crystal, *Phys Rev Lett* 112(14) (2014) 145504.
- 425 [10] C.F. Robertson, M.C. Fivel, A study of the submicron indent-induced plastic  
426 deformation, *Journal of Materials Research* 14(6) (1999) 2251-2258.
- 427 [11] T. Tsuru, Y. Shibutani, Anisotropic effects in elastic and incipient plastic deformation  
428 under (001), (110), and (111) nanoindentation of Al and Cu, *Physical Review B* 75(3) (2007).
- 429 [12] J. Li, K.J. Van Vliet, T. Zhu, S. Yip, S. Suresh, Atomistic mechanisms governing elastic  
430 limit and incipient plasticity in crystals, *Nature* 418(6895) (2002) 307-310.

- 431 [13] S. Jiao, W. Tu, P. Zhang, W. Zhang, L. Qin, Z. Sun, J. Chen, Atomistic insights into the  
432 prismatic dislocation loop on Al (1 0 0) during nanoindentation investigated by molecular  
433 dynamics, *Computational Materials Science* 143 (2018) 384-390.
- 434 [14] S. Graça, P.A. Carvalho, R. Colaço, Dislocation structures in nanoindented ductile  
435 metals—a transmission electron microscopy direct observation, *Journal of Physics D:  
436 Applied Physics* 44(33) (2011) 335402.
- 437 [15] A. Minor, J. Morris Jr, E. Stach, Quantitative in situ nanoindentation in an electron  
438 microscope, *Applied Physics Letters* 79(11) (2001) 1625-1627.
- 439 [16] S. Lee, A. Vaid, J. Im, B. Kim, A. Prakash, J. Guenole, D. Kiener, E. Bitzek, S.H. Oh,  
440 In-situ observation of the initiation of plasticity by nucleation of prismatic dislocation loops,  
441 *Nat Commun* 11(1) (2020) 2367.
- 442 [17] M.F. Ashby, L. Johnson, On the generation of dislocations at misfitting particles in a  
443 ductile matrix, *Philosophical Magazine* 20(167) (1969) 1009-1022.
- 444 [18] T. Filleter, R. Bennewitz, Nanometre-scale plasticity of Cu(100), *Nanotechnology* 18(4)  
445 (2007) 044004.
- 446 [19] M. Dupraz, G. Beutier, T.W. Cornelius, G. Parry, Z. Ren, S. Labat, M.I. Richard, G.A.  
447 Chahine, O. Kovalenko, M. De Boissieu, E. Rabkin, M. Verdier, O. Thomas, 3D Imaging of  
448 a Dislocation Loop at the Onset of Plasticity in an Indented Nanocrystal, *Nano Lett* 17(11)  
449 (2017) 6696-6701.
- 450 [20] Y. Gaillard, C. Tromas, J. Woïrgard, Study of the dislocation structure involved in a  
451 nanoindentation test by atomic force microscopy and controlled chemical etching, *Acta  
452 Materialia* 51 (2003) 1059-1065.
- 453 [21] A.M. Minor, E.T. Lilleodden, E.A. Stach, J.W. Morris, Direct observations of incipient

- 454 plasticity during nanoindentation of Al, *Journal of Materials Research* 19(01) (2011) 176-  
455 182.
- 456 [22] A.M. Minor, S.A. Asif, Z. Shan, E.A. Stach, E. Cyrankowski, T.J. Wyrobek, O.L.  
457 Warren, A new view of the onset of plasticity during the nanoindentation of aluminium, *Nat*  
458 *Mater* 5(9) (2006) 697-702.
- 459 [23] Y. Mishin, D. Farkas, M.J. Mehl, D.A. Papaconstantopoulos, Interatomic potentials for  
460 monoatomic metals from experimental data and ab initio calculations, *Physical Review B*  
461 59(5) (1999) 3393-3407.
- 462 [24] M. Parrinello, A. Rahman, Crystal Structure and Pair Potentials: A Molecular-Dynamics  
463 Study, *Physical Review Letters* 45(14) (1980) 1196-1199.
- 464 [25] K. Durst, B. Backes, M. Göken, Indentation size effect in metallic materials: Correcting  
465 for the size of the plastic zone, *Scripta Materialia* 52(11) (2005) 1093-1097.
- 466 [26] C.R. Taylor, E.A. Stach, G. Salamo, A.P. Malshe, Nanoscale dislocation patterning by  
467 ultralow load indentation, *Applied Physics Letters* 87(7) (2005) 073108.
- 468 [27] A. Eikum, G. Thomas, Precipitation and dislocation nucleation in quench-aged Al-Mg  
469 alloys, *Acta Metallurgica* 12(5) (1963) 537-545.
- 470 [28] R.S. Barnes, D.J. Mazey, Stress-generated prismatic dislocation loops in quenched  
471 copper, *Acta Metallurgica* 11(4) (1963) 281-286.
- 472 [29] R. Bullough, R.C. Newman, The spacing of prismatic dislocation loops, *Philosophical*  
473 *Magazine* 5(57) (1960) 921-926.
- 474 [30] X.J. Xin, G.S. Daehn, R.H. Wagoner, Equilibrium configuration of coaxial prismatic  
475 dislocation loops and related size-dependent plasticity, *Acta Materialia* 45(5) (1997) 1821-  
476 1836.

- 477 [31] S.G. Srinivasan, X.Z. Liao, M.I. Baskes, R.J. McCabe, Y.H. Zhao, Y.T. Zhu, Compact  
478 and dissociated dislocations in aluminum: implications for deformation, *Phys Rev Lett* 94(12)  
479 (2005) 125502.
- 480 [32] I. Shin, E.A. Carter, Possible origin of the discrepancy in Peierls stresses of fcc metals:  
481 First-principles simulations of dislocation mobility in aluminum, *Physical Review B* 88(6)  
482 (2013).
- 483 [33] T. Kosugi, T. Kino, A new internal friction peak and the problem of the Peierls potential  
484 in f.c.c. metals, *Materials Science & Engineering A* 164(1-2) (1993) 368-372.
- 485 [34] J.N. Wang, Prediction of Peierls stresses for different crystals, *Materials Science and*  
486 *Engineering A* 206 (1996) 259-269.
- 487 [35] J. Gagel, D. Weygand, P. Gumbsch, Formation of extended prismatic dislocation  
488 structures under indentation, *Acta Materialia* 111 (2016) 399-406.
- 489 [36] T.P. Remington, C.J. Ruestes, E.M. Bringa, B.A. Remington, C.H. Lu, B. Kad, M.A.  
490 Meyers, Plastic deformation in nanoindentation of tantalum: A new mechanism for prismatic  
491 loop formation, *Acta Materialia* 78 (2014) 378-393.
- 492 [37] F. Seitz, Prismatic Dislocations and Prismatic Punching in Crystals, *Physical Review*  
493 79(4) (1950) 723-724.
- 494 [38] Y. Shibutani, T. Tsuru, A. Koyama, Nanoplastic deformation of nanoindentation:  
495 Crystallographic dependence of displacement bursts, *Acta Materialia* 55(5) (2007) 1813-  
496 1822.
- 497 [39] H. Yu, A.C.F. Cocks, E. Tarleton, Formation of prismatic dislocation loops during  
498 unloading in nanoindentation, *Scripta Materialia* 189 (2020) 112-116.
- 499 [40] F.F. Csikor, C. Motz, D. Weygand, M. Zaiser, S. Zapperi, Dislocation avalanches, strain

500 bursts, and the problem of plastic forming at the micrometer scale, *Science* 318(5848) (2007)  
501 251-254.

502 [41] P.D. Ispanovity, L. Laurson, M. Zaiser, I. Groma, S. Zapperi, M.J. Alava, Avalanches  
503 in 2D dislocation systems: plastic yielding is not depinning, *Phys Rev Lett* 112(23) (2014)  
504 235501.

505 [42] W. Zielinski, H. Huang, W.W. Gerberich, Microscopy and microindentation mechanics  
506 of single crystal Fe-3 wt. % Si: Part II. TEM of the indentation plastic zone, *Journal of*  
507 *Materials Research* 8(6) (1993) 1300-1310.

508 [43] H.B. X. Cai, Hardness measurements of thin films-determining depth to thickness using  
509 FEM, *Thin Solid Films* 264 (1995) 59-71.

510 [44] B. Bhushan, V.N. Koinkar, Nanoindentation hardness measurements using atomic force  
511 microscopy, *Applied physics letters* 64(13) (1994) 1653-1655.

512 [45] B.R. Neugirg, S.R. Koebley, H.C. Schniepp, A. Fery, AFM-based mechanical  
513 characterization of single nanofibres, *Nanoscale* 8(16) (2016) 8414-26.

514 [46] R. Saha, W.D. Nix, Effects of the substrate on the determination of thin film mechanical  
515 properties by nanoindentation, *Acta Materialia* 50(1) (2002) 23-38.

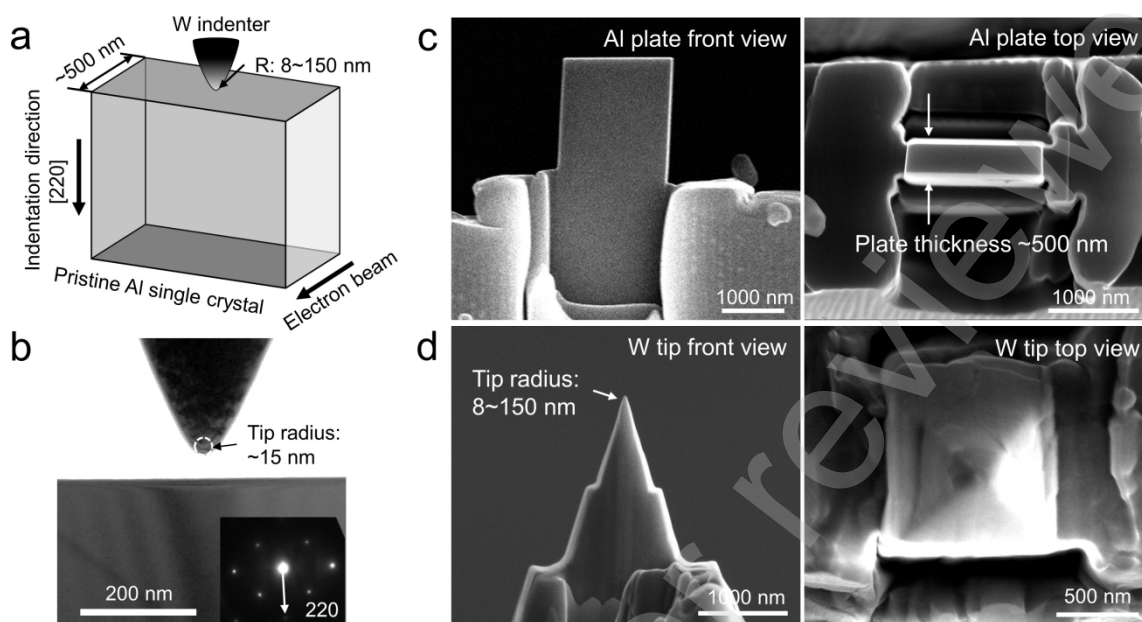
516 [47] K.M. Atsutomo Nakamura, Jun Tohma, Takahisa Yamamoto & Yuichi Ikuhara,  
517 Conducting nanowires in insulating ceramics., *Nature Materials* 2 (2003) 453-456.

518

519

520

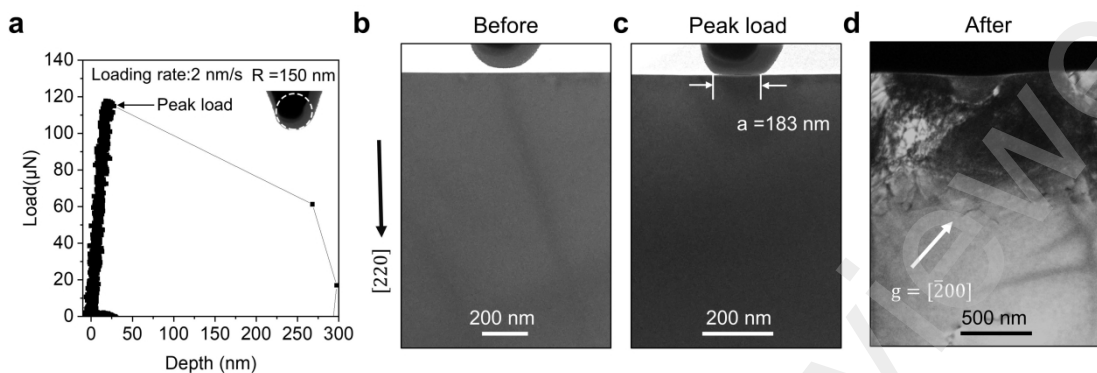




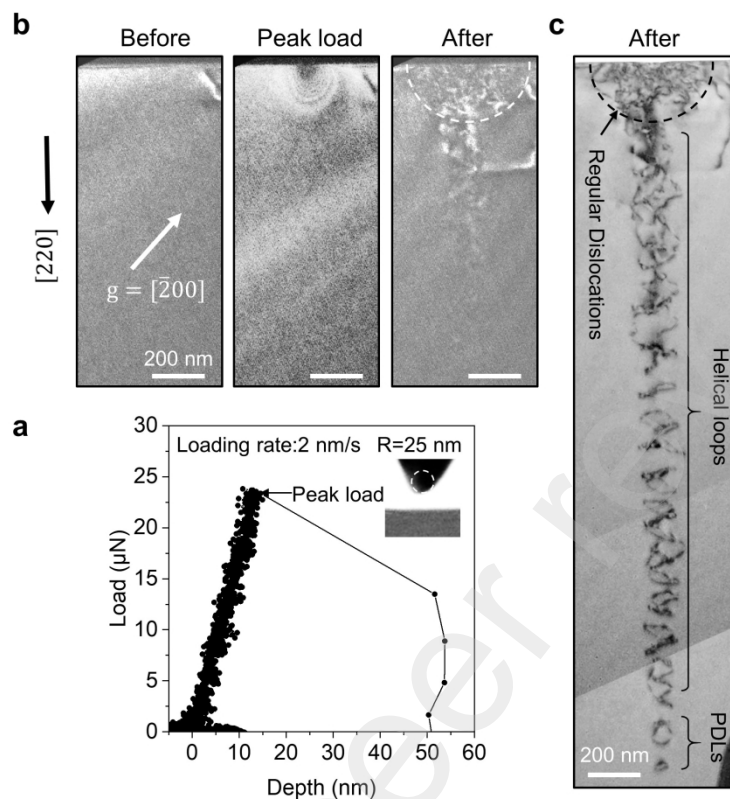
521  
522

**Figure 1. The experimental setup for *in situ* nanoindentation.** (a). Schematic illustration showing mechanical testing setup. (b). The bright field TEM image of the tungsten indenter and the single crystalline Al plate with nearly pristine interior. The inset is the diffraction pattern of the Al specimen ([002] zone axis and indentation direction along [220]). (c). SEM images showing aluminum samples. Side view (left) and top view (right) of a typical Al plate. the plate thickness was measured to be ~500 nm. (d). SEM images showing side view (left) and top view (right) of a typical as-prepared tungsten tip, the FIB fabricated tip radius ranges from 8 to 150 nm.

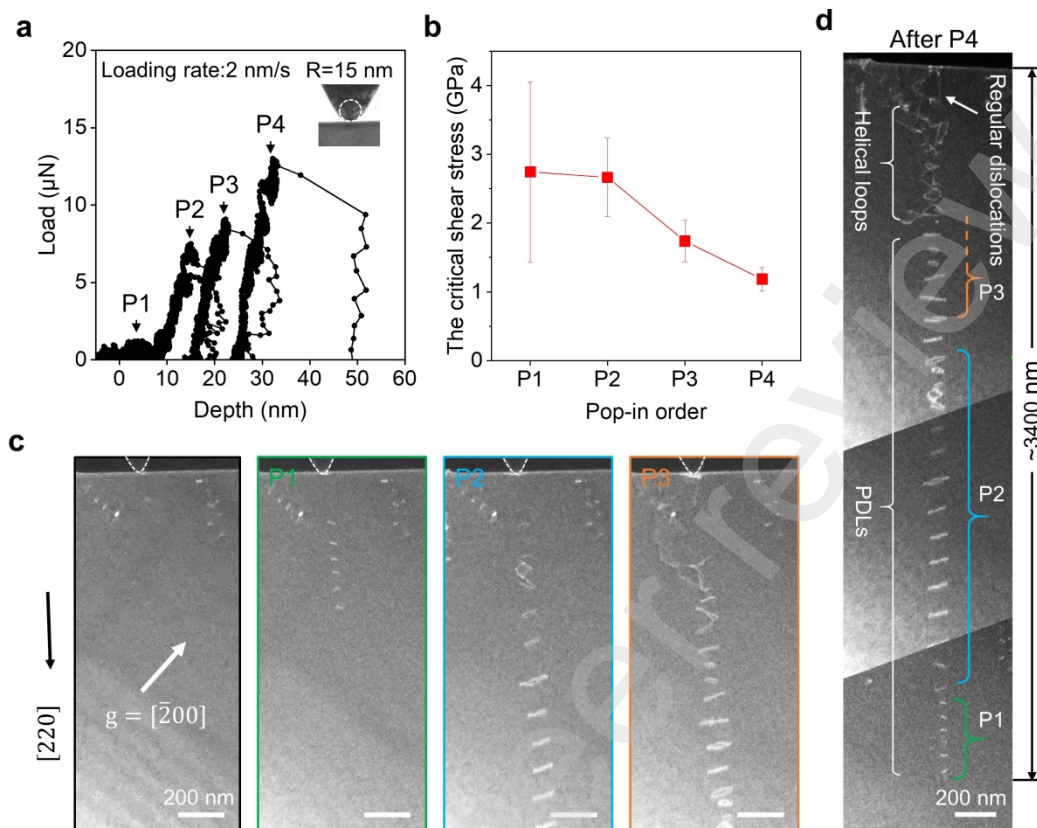
529  
530



531  
 532 **Figure 2.** Three-dimensional plastic zone (3D PZ) formed with the indenter tip radius of  
 533 150 nm. (a). The load-depth curve. The upper right inset shows the TEM image of the  
 534 indenter tip. (b). Bright-field image showing the dislocation structure before the  
 535 indentation. (c). The frame extracted from indentation video at the peak load, as marked on  
 536 the load-depth curve just before the pop-in, showing purely elastic response to the loading.  
 537 (d) The dark-field image taken with  $[\bar{2}00]$  diffraction vector showing the dislocation  
 538 structure after the indentation.

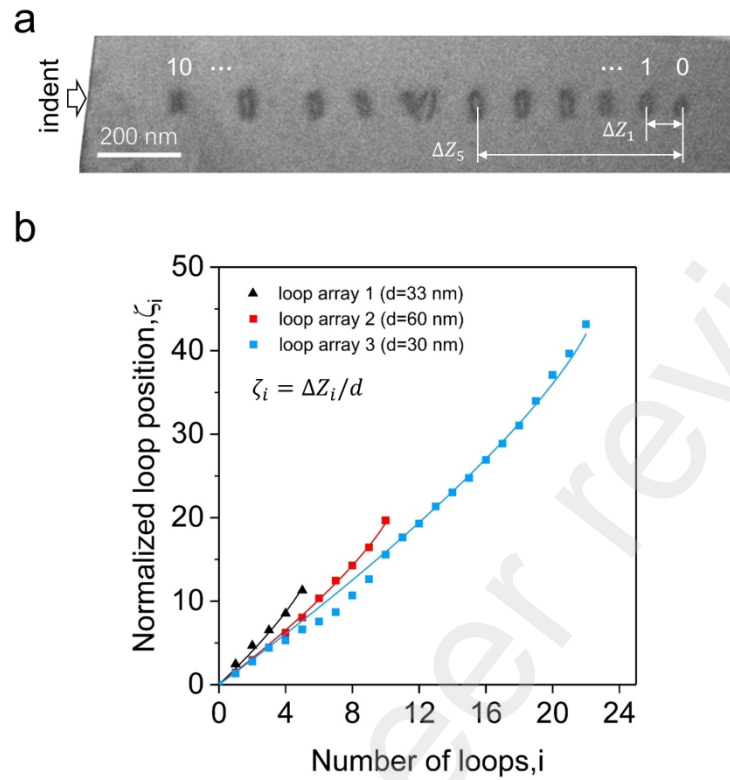


539  
 540 **Figure 3.** Three-dimensional plastic zone plus one-dimensional plastic zone (3D+1D PZ)  
 541 formed during *in situ* indentation with a tip of radius of 25 nm. (a). The load-depth curve  
 542 (b). Dark-field images taken with  $[\bar{2}00]$  diffraction vector showing the evolution of  
 543 dislocation configuration with increasing indentation. The sample exhibited obvious elastic  
 544 stress field contrast underneath the indenter at time  $t_p$ , corresponding to peak load as  
 545 marked on the load-depth curve. (c). Bright-field image taken after indentation, showing  
 546 dislocation configuration below the indent.  
 547

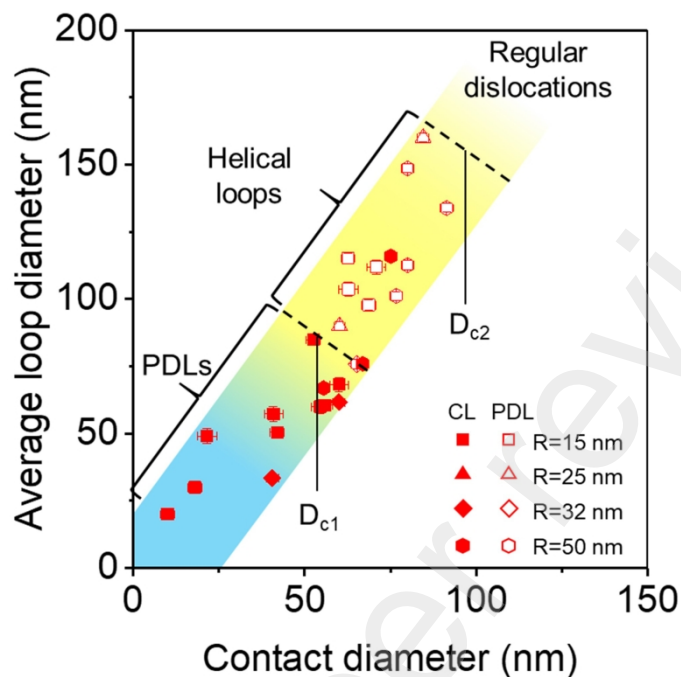


548

549 **Figure 4.** The formation of one-dimensional plastic zone (1D PZ) during *in situ* indentation  
 550 with a tip radius of 15 nm. (a). The load-depth curve. Four yielding events are indicated by  
 551 arrows P1 to P4. (b). The critical shear stress at each yielding point. (c). Dark-field images  
 552 of the dislocation configuration after each corresponding yielding event as indicated at the  
 553 depth-load curve; the diffraction vector is  $[\bar{2}00]$ . (d). Overview image stitched together  
 554 using four images, showing the dislocation structure below the indenter after indentation.

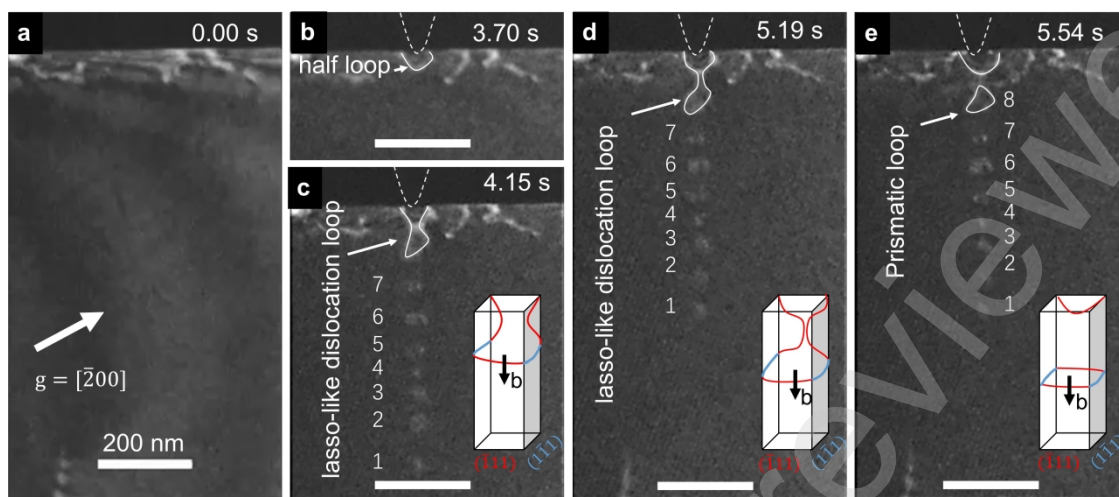


555 **Figure 5. Configuration of coaxial prismatic dislocation loops and the fitting results.**  
 556  
 557 (a). TEM image of a set of PDLs in an array,  $\zeta_i$  is used to represent the position of loop  $i$   
 558 from the first leading loop (normalized by average loop diameter  $d$ ). (b). the normalized  
 559 loop position for each PDL. The lines represent the fitting results using the equation (1).

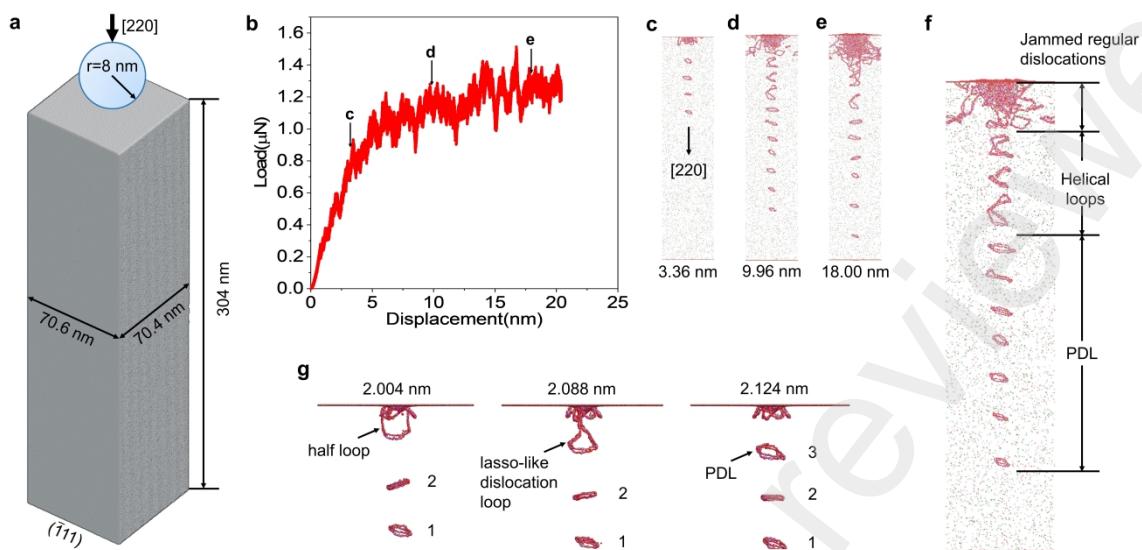


560

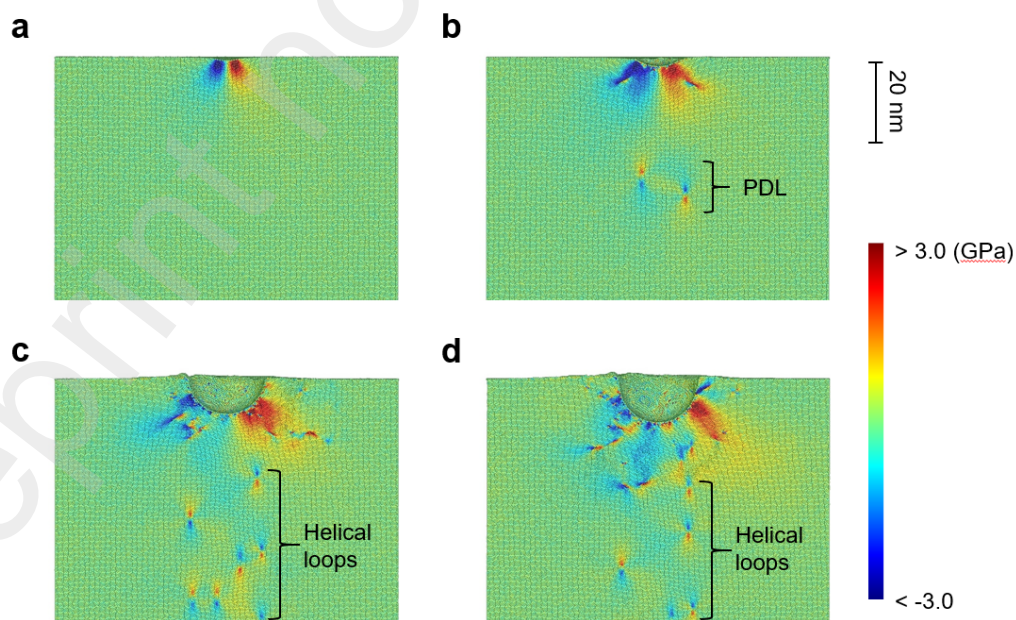
561 **Figure 6. The relationship between the indent contact radius and loop radius/types.** The  
 562 size of the points represents the initial indenter tip radius. When the contact diameter is  
 563 smaller than  $\sim 50$  nm, PDLs are favorable; closed helical loops are more favorable otherwise.  
 564 The indent contact radius is measured directly from *in situ* video frames just before the  
 565 yielding events.



566  
 567 **Figure 7. The formation process of an individual PDL.** (a). Dark-field TEM image of the  
 568 single crystal Al plate before the indentation. (b). The nucleation of a half loop underneath  
 569 the indenter, indicated by a white arrow. (c-d). Formation of a lasso-like dislocation loop  
 570 attached to the half loop. (e). A new PDL is released when the two dislocation segments  
 571 meet and react. Insets in c-e schematically illustrate the dislocation shapes in the  
 572 corresponding images, compared with the glide prism bounded by four  $\{111\}$  planes. All  
 573 scale bars represent 200 nm



574  
 575 **Figure 8 MD-simulated dislocation generation, during nanoindentation using an 8-nm**  
 576 **radius sphere on aluminum along [220] direction.** (a). Simulation model. (b). Load-  
 577 displacement curve. (c-e). Snapshots of at different stages of the nanoindentation depth.  
 578 Dislocations are detected by central symmetry parameter coloring. (f). The overview image of  
 579 emitted dislocations. (g). The simulated formation process of a PDL.

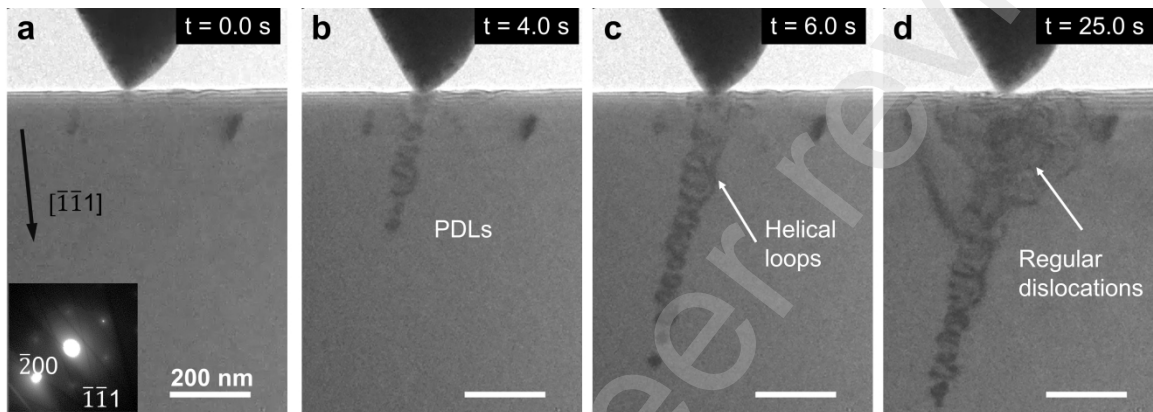


580



581 **Figure 9** The distributions of resolved shear stress on the  $(\bar{1}\bar{1}1)[110]$  slip system  
 582 **during nanoindentation MD simulation with an indenter radius of 8 nm.** (a). The  
 583 elastic stage before dislocation generation. (b). The PDL emission stage. (c). The helical  
 584 loop emission stage. (d). The regular dislocation generation stage.

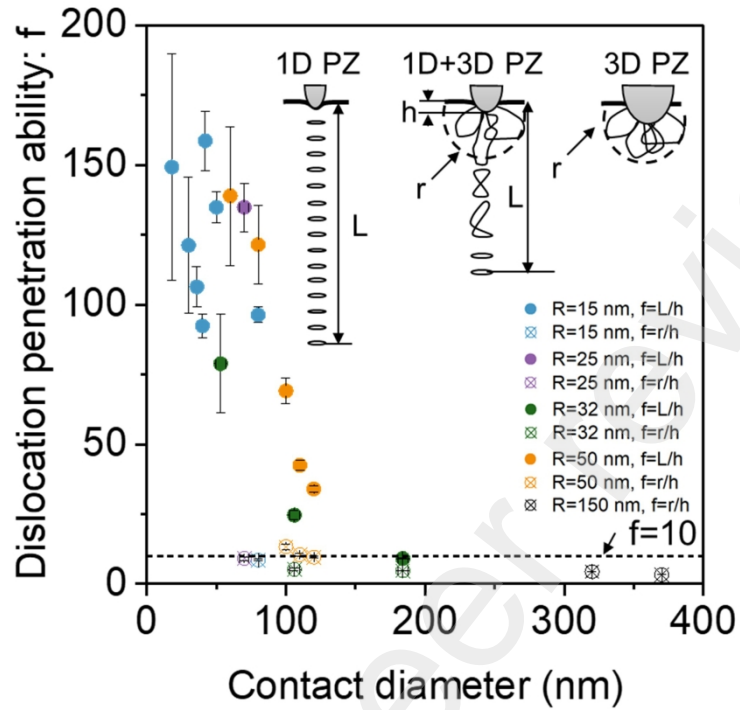
585



586

587 **Figure 10.** The evolution of dislocation configuration when an indentation is made  
 588 **along the  $[\bar{1}\bar{1}1]$  direction of aluminum crystal.** (a). Image showing the indenter and  
 589 aluminum sample before engaging the tip. (b-d). The image series showing dislocation  
 590 structure at different moments of indentation. Time labels are at the top of each image.

591



592  
 593 **Figure 11. Dislocation penetration ability  $f$  versus the contact area.** Here the dislocation  
 594 penetration ability factor, as shown in the inset: is evaluated using  $f=L/h$  for PDLs/helices  
 595 (solid circles), and  $f=r/h$  for jammed regular dislocations (hollow circles), where  $L$ ,  $r$  and  $h$   
 596 are marked in the inset.

597

598